AGU PUBLICATIONS

Journal of Advances in Modeling Earth Systems

RESEARCH ARTICLE

10.1002/2014MS000356

Resolution-dependent behavior of subgrid-scale vertical transport in the Zhang-McFarlane convection parameterization

Heng Xiao[1], William I. Gustafson Jr.[1], Samson M. Hagos[1], Chien-Ming Wu[2], and Hui Wan[1]

[1]Atmospheric Sciences and Global Change Division, Pacific Northwest National Laboratory, Richland, Washington, USA, [2]Department of Atmospheric Sciences, National Taiwan University, Taipei, Taiwan

Key Points:
- ZM convective transport resolution-dependence is determined by QE closure
- Simple modification of closure improves significantly the resolution dependence

Correspondence to:
H. Xiao,
heng.xiao@pnnl.gov

Citation:
Xiao, H., W. I. Gustafson Jr., S. M. Hagos, C.-M. Wu, and H. Wan (2015), Resolution-dependent behavior of subgrid-scale vertical transport in the Zhang-McFarlane convection parameterization, *J. Adv. Model. Earth Syst.*, *7*, 537–550, doi:10.1002/2014MS000356.

Received 19 JUN 2014
Accepted 9 MAR 2015
Accepted article online 16 MAR 2015
Published online 18 APR 2015

Abstract To better understand the behavior of quasi-equilibrium-based convection parameterizations at higher resolution, we use a diagnostic framework to examine the resolution-dependence of subgrid-scale vertical transport of moist static energy as parameterized by the Zhang-McFarlane convection parameterization (ZM). Grid-scale input to ZM is supplied by coarsening output from cloud-resolving model (CRM) simulations onto subdomains ranging in size from 8×8 to 256×256 km^2. Then the ZM-based parameterization of vertical transport of moist static energy for scales smaller than the subdomain size ($\overline{w'h'}_{ZM}$) are compared to those directly calculated from the CRM simulations ($\overline{w'h'}_{CRM}$) for different subdomain sizes. The ensemble mean $\overline{w'h'}_{CRM}$ decreases by more than half as the subdomain size decreases from 128 to 8 km across while $\overline{w'h'}_{ZM}$ decreases with subdomain size only for strong convection cases and increases for weaker cases. The resolution dependence of $\overline{w'h'}_{ZM}$ is determined by the positive-definite grid-scale tendency of convective available potential energy (CAPE) in the convective quasi-equilibrium (QE) closure. Further analysis shows the actual grid-scale tendency of CAPE (before taking the positive definite value) and $\overline{w'h'}_{CRM}$ behave very similarly as the subdomain size changes because they are both tied to grid-scale advective tendencies. We can improve the resolution dependence of $\overline{w'h'}_{ZM}$ significantly by averaging the grid-scale tendency of CAPE over an appropriately large area surrounding each subdomain before taking its positive definite value. Even though the ensemble mean $\overline{w'h'}_{CRM}$ decreases with increasing resolution, its variability increases dramatically. $\overline{w'h'}_{ZM}$ cannot capture such increase in the variability, suggesting the need for stochastic treatment of convection at relatively high spatial resolution (8 or 16 km).

1. Introduction

Moist convection is a crucial component of the global atmospheric circulation. Because the spatial resolution of atmospheric general circulation models (GCMs; ~100 km in the horizontal for current generation models) is too coarse to explicitly represent the dynamics of individual convective clouds, moist convection is usually parameterized.

The development of convection parameterization for atmospheric models started more than half a century ago and huge progress has been made since then [see *Arakawa*, 2004 for a recent review]. Among many other achievements along the way, the "moist-convective quasi equilibrium" (QE hereafter) hypothesis proposed by *Arakawa and Schubert* [1974, AS74 hereafter] is an influential concept for almost all subsequent convection parameterizations [see also *Yano and Plant*, 2012].

In the context of convection parameterizations, the original QE hypothesis states that if the timescale of convective adjustment is much shorter than the timescale of large-scale processes in the environment, then the atmosphere goes through a series of quasi equilibria with respect to moist convection as the destabilization by large-scale processes is quickly removed by convective adjustment. In convection parameterizations, the idea of QE is usually expressed in terms of the convective available potential energy (CAPE or simply A) in the following way. Given

$$\frac{dA}{dt} = \left(\frac{dA}{dt}\right)_g + \left(\frac{dA}{dt}\right)_s, \tag{1}$$

and

© 2015. The Authors.
This is an open access article under the terms of the Creative Commons Attribution-NonCommercial-NoDerivs License, which permits use and distribution in any medium, provided the original work is properly cited, the use is non-commercial and no modifications or adaptations are made.

$$\left|\left(\frac{dA}{dt}\right)_g\right| \gg \left|\frac{dA}{dt}\right|, \left|\left(\frac{dA}{dt}\right)_s\right| \gg \left|\frac{dA}{dt}\right|, \tag{2}$$

then

$$-\left(\frac{dA}{dt}\right)_s \approx \left(\frac{dA}{dt}\right)_g, \tag{3}$$

where we use subscript "g" to denote CAPE change due to grid-scale processes—equivalent to the large-scale processes in the conceptual development of QE—and "s" to denote CAPE change due to subgrid-scale processes, equivalent to the convective adjustments. A or CAPE is defined as

$$A = \int_{p_t}^{p_b} R_d (T_{vp} - \bar{T}_v)\, d\ln p, \tag{4}$$

where R_d is the gas constant for dry air, T_{vp} is the virtual temperature of an air parcel moving upward (usually adiabatically) from near the surface (essentially a certain parcel initiation level), and $\bar{T}_v$ is the virtual temperature of the environment, usually taken to be that of the grid-box mean in a parameterization. p_b and p_t are the pressures at the parcel initiation level and at the level of neutral buoyancy, respectively. Alternatively, A can be replaced by other measures of vertically integrated buoyancy for a rising parcel, like the cloud work function used by AS74. In the context of convection parameterizations, the term "large-scale processes" is often used to denote processes other than those treated by the convection parameterization, including both grid-scale advection and other processes parameterized using grid-scale variables, like radiation, surface and planetary boundary layer (PBL) processes. For clarity, we will refer to these nonconvective processes as environmental processes.

The accuracy of the original QE hypothesis rests upon the degree of separation of scales in space and time between convective and environmental processes [see, e.g., AS74; *Lord and Arakawa*, 1980]. Recent studies by *Yano et al*. [2000] and *Neelin et al*. [2008], however, claim that there is no characteristic time scale for convective adjustment, which makes the separation of time scales questionable. *Mapes* [1997] also argues that since gravity waves excited by convective heating can traverse a typical GCM grid box very quickly (in less than 1 h), diagnostic evidence for equation (2) found in observational and modeling studies using time averages of dA/dt and $(dA/dt)_g$ [e.g., *Xu and Arakawa*, 1992] cannot be seen as a proof of the original QE hypothesis [see also *Arakawa*, 2004, section 5e], although his argument does not disprove the original QE hypothesis either.

In recent studies [e.g., *Neelin et al*., 2008; *Plant and Craig*, 2008], the QE hypothesis is more often interpreted as a statistical balance between environmental and convective processes in a convecting air column, which is an idea that goes back to the beginning of convection parameterization studies [see also *Arakawa*, 2004], rather than a deterministic and causal relationship between large-scale forcing and convective adjustment. *Plant and Craig* [2008] assume a statistical equilibrium between an ensemble of noninteracting convective elements described by a stochastic model, and its environment. Even though the statistical properties of the assumed equilibrium are still derived using the original QE concept, the existence of the equilibrium is supported by "the law of large numbers" in statistical mechanics (i.e., a large number of convective elements, see also *Williams* [2005]). *Neelin et al*. [2008] demonstrated that even though QE can describe the observed relationship between precipitation and the tropical atmospheric state (given by column integrated moisture or CAPE) in a statistical sense, there is significant deviation from a deterministic QE even if we average over a large domain (200 km). This again supports the consideration of a stochastic (nondeterministic) parameterization for convection.

Both the original mechanistic and the more recent statistical interpretations of QE assume it operates over a large ensemble of convective elements, i.e., over a horizontal domain that contains such a large ensemble (usually taken to be several hundred kilometers in each direction). Therefore, convection parameterizations based on QE are generally not designed with resolution-awareness in mind. This means that as they are applied at higher and higher resolutions, there is no guarantee that these parameterizations will automatically account for the changing partition between grid-scale and subgrid-scale transports (and sources/sinks) of heat and moisture as resolution changes [see, e.g., *Jung and Arakawa*, 2004]. Most likely, due to various simplifying assumptions specific to coarse resolutions, parameterizations will overestimate the subgrid-

scale effects and "double-count" some portion of the overall convective adjustment when model resolution is increased from what the parameterizations are designed for. This potential double-counting problem is the subject of a recent study by *Arakawa and Wu* [2013, see also *Wu and Arakawa*, 2014], in which they proposed a way to remove double-counting by scaling down the "full" convective transport calculated from the original QE closure using a diagnosed convective updraft fraction.

In the present study, we perform a detailed analysis of the resolution-dependent behavior of subgrid-scale vertical transport produced by a QE-based convection parameterization, namely the Zhang-McFarlane convection parameterization [*Zhang and McFarlane*, 1995, ZM hereafter]. Based on our analysis, we propose a simple algorithm to avoid double-counting and improve the resolution dependence of parameterized subgrid-scale vertical transport under the QE framework. Our results also emphasize the need for stochastic formulations to improve the representation of convective variability at high resolutions.

2. Methodology

Moist static energy (h) is defined as $h = c_pT + gz + Lq_v$, where c_p is the specific heat of air at constant pressure, T is temperature, g is gravity, z is height, L is the latent heat of vaporization, and q_v is water vapor mixing ratio. In a large-scale numerical model, the budget equation for grid mean h, $\bar{h}$, can be written as follows,

$$\rho\frac{\partial\bar{h}}{\partial t} = -\rho(\bar{u}\frac{\partial\bar{h}}{\partial x} + \bar{v}\frac{\partial\bar{h}}{\partial y} + \bar{w}\frac{\partial\bar{h}}{\partial z}) - \frac{\partial}{\partial z}(\rho\overline{w'h'}) + \bar{H}, \tag{5}$$

where ρ is the grid mean air density, $\bar{u}$, $\bar{v}$, $\bar{w}$ are the grid mean velocities, and $\bar{H}$ is a place holder for diabatic heating terms. The second term on the right-hand side is the vertical divergence of $\overline{w'h'}$, the subgrid-scale vertical transport of h, or convective transport of h, as commonly referred to in convection parameterization literature. This term represents the effect of unresolved convective mixing on the mean state, and it will be the focus of our analysis. We assume that the horizontal divergence of eddy flux in the model grid box is negligible when deriving equation (5).

Our analysis consists mainly of comparing, at different resolutions, $\overline{w'h'}$ calculated directly from CRM simulations (referred to as $\overline{w'h'}_{CRM}$ hereafter) with $\overline{w'h'}$ parameterized by the ZM parameterization in a diagnostic single column model (SCM)-like setup (referred to as $\overline{w'h'}_{ZM}$ hereafter), where the input to ZM, i.e., the grid-mean state variables and advective tendencies, are calculated from the same CRM simulations.

2.1. CRM Simulations

We analyze simulations of tropical convection from two different CRMs.

2.1.1. Idealized Simulation of Tropical Convection

The first CRM simulation we analyze is the case with background shear analyzed in *Arakawa and Wu* [2013]. This is an idealized case with thermodynamic forcings (i.e., vertical profiles of heating and moistening) based on the Global Atmospheric Research Program (GARP) Atlantic Tropical Experiment (GATE) phase III. The CRM is the 3-D vorticity equation model of *Jung and Arakawa* [2008] with a three-phase cloud microphysics parameterization [*Krueger et al*., 1995]. The horizontal domain is 512 $\times$ 512 km^2 with periodic boundary conditions. The horizontal grid spacing is 2 km. There are 34 layers in the vertical with model top at approximately 19 km. The lowest model layer is 100 m deep. The lower boundary condition is ocean surface with fixed temperature at 300 K. A constant cooling rate of 2 K d^{-1} is specified to mimic radiative cooling. The winds are nudged toward a prescribed profile typical of Tropical Ocean and Global Atmosphere Coupled Ocean–Atmosphere Response Experiment (TOGA COARE) with a 2 h time scale. The readers are referred to *Arakawa and Wu* [2013] and *Jung and Arakawa* [2010] for more details on the setup.

The simulation is 24 h long with constant forcing. We analyze snapshots taken at 20 min intervals from the last 12 h of the simulation, when the simulated convection reaches a quasi-steady state. The mean precipitation rate is 2.58 mm d^{-1} over the analyzed period. We will refer to this simulation as IDEAL.

2.1.2. Simulation of Tropical Convection in the DYNAMO Period

The second CRM simulation is performed with the Weather Research and Forecasting (WRF) [*Skamarock et al*., 2008] model (version 3.4.1). The horizontal domain is 1100 $\times$ 1100 km^2 and covers the area from

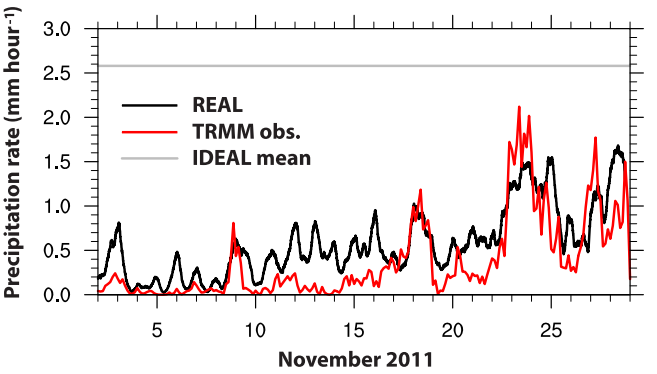

Figure 1. Domain-averaged precipitation rate (mm h^{-1}) time series from REAL (black) and TRMM satellite observation (red). The gray line indicates the mean precipitation rate from the last 12 h of the IDEAL case.

approximately 6°S to 4°N and 68°E to 78°E in the equatorial Indian Ocean using horizontal grid spacing of 2 km. There are 28 vertical layers with the model top at approximately 20 km. The lowest model layer is approximately 100 m deep. The simulation uses the Rapid Radiative Transfer Model for General Circulation Models (RRTMG) [*Iacono et al*., 2000] for longwave radiation, *Dudhia* [1989] for short-wave radiation, the Morrison 2 moment scheme [*Morrison et al*., 2005] for microphysics, and the University of Washington PBL scheme [*Bretherton and Park*, 2009]. The lateral and lower boundary conditions are supplied by ERA-interim 6 hourly analyses. The simulation period is 1–28 November 2011. Temporal snapshots are written out every 10 min.

The geographical region and time period of the simulation is chosen such that comparisons with in situ observations collected during the 2011 Atmospheric Radiation Measurement (ARM) Madden Julian Oscillation (MJO) Investigation Experiment (AMIE) and Dynamics of the MJO (DYNAMO) field campaign (October 2011 to February 2012) [*Yoneyama et al*., 2013] can be made. *Hagos et al*. [2014a, 2014b] compared WRF simulations with almost identical setups against both satellite observation and in situ radar measurements collected during the AMIE/DYNAMO campaign and found good agreement in terms of precipitation, cloud, and cold pool features associated with convective activities.

We will refer to this second simulation as REAL. Figure 1 shows the time series of domain-averaged precipitation rate from REAL together with Tropical Rainfall Measuring Mission (TRMM, 3B42 product) satellite observations [*Huffman et al*., 2007]. The simulation tends to overestimate precipitation during the drier part of the month but reproduces the timing and strength of strong deep convection episodes in the domain relatively realistically. We also see that the precipitation rate in REAL is always less than that in IDEAL, indicating stronger convection in IDEAL. There is considerable precipitation variability within REAL because of the time-varying forcing. An MJO event propagates into the model domain around 22 November, giving rise to several strong precipitation episodes. In IDEAL, there is little variability in precipitation due to its constant forcing.

We choose to use 2 km grid spacing, which is common among recent work on similar topics. But, studies have shown that simulations with this grid spacing still can produce unrealistic features of cloud-scale turbulence compared to simulations using grid spacings on the order of 100 m [e.g., *Bryan et al*., 2003].

2.1.3. Evaluating $\overline{w'h'}_{CRM}$

To evaluate $\overline{w'h'}$ at different resolutions from these CRM simulations, we follow the basic procedure of *Arakawa and Wu* [2013]. First we divide the CRM domain into equal-size subdomains and then define $\bar{w}$, $\bar{h}$, and $\overline{wh}$ in each subdomain as averages of w, h, and wh over all CRM grid points in the subdomain. Then $\overline{w'h'}_{CRM}$ is given by $\overline{wh}-\bar{w}\bar{h}$. $\overline{w'h'}_{CRM}$ is calculated this way at different resolutions (i.e., different subdomain sizes, 8×8, 16×16, 32×32, 64×64, 128×128, and 256 × 256 km^2).

2.2. The Zhang-McFarlane Convection Parameterization and the Calculation of $\overline{w'h'}_{ZM}$

ZM parameterizes the convective transport term in equation (5) as

$$\rho\overline{w'h'}=M_u(h_u-\bar{h})+M_d(h_d-\bar{h}), \tag{6}$$

where h_u and h_d are in-updraft and in-downdraft moist static energy, M_u and M_d are the bulk updraft and downdraft mass fluxes (see equation (1) in ZM). In ZM, the mass flux model calculates all the unknowns in equation (6) once the cloud-base updraft mass flux M_b is given. M_b is calculated using a variant of equation (3):

$$M_b F = \frac{\max(A - A_0, 0)}{\tau}, \tag{7}$$

where F is the rate of CAPE (A) removal by convection per unit M_b, and is given by the mass flux model; A_0 is an empirical constant representing the "equilibrium state" CAPE; and τ is the convective adjustment time scale, also a constant. The left-hand side of equation (7) can be seen as $-(dA/dt)_s$, i.e., the removal of CAPE by subgrid-scale convective processes, while the right-hand side can be interpreted as a simple approximation to $(dA/dt)_g$, where a fixed convective adjustment time and a fixed "equilibrium state" CAPE is assumed. Equation (7) is the so-called "closure equation" in ZM.

Following previous diagnostic evaluations of QE-based convection parameterizations like *Lord* [1982] and *Xu and Arakawa* [1992], we use the following variant of equation (7)) as the closure:

$$M_b F = \left(\frac{dA}{dt}\right)_{g+} \equiv \max\left[\left(\frac{dA}{dt}\right)_g, 0\right] \tag{8}$$

$(dA/dt)_g$ includes contributions from environmental processes like surface forcing, radiative heating, and grid-scale advection, as discussed in *Emanuel* [1994, pp. 480–483] and *Zhang* [2003]:

$$\left(\frac{dA}{dt}\right)_g \approx R_d \int_{p_t}^{p_b} \frac{\partial T_{vp}}{\partial t} d\ln p - R_d \int_{p_t}^{p_b} \frac{\partial \bar{T}_v}{\partial t} d\ln p \approx (\bar{T}_b - \bar{T}_t)\frac{c_p}{\bar{\theta}_{eb}}\frac{\partial \bar{\theta}_{eb}}{\partial t} - R_d \int_{p_t}^{p_b} \left[\left(\frac{\partial \bar{T}_v}{\partial t}\right)_R + \left(\frac{\partial \bar{T}_v}{\partial t}\right)_G\right] d\ln p, \tag{9}$$

where $\bar{T}_b$ and $\bar{T}_t$ are mean temperatures at the parcel initiation level and at the level of neutral buoyancy, respectively, and $\bar{\theta}_{eb}$ is the mean equivalent potential temperature at the parcel initiation level, where the mean is defined over the particular subdomain being analyzed. The first term on the right-hand side comes mainly from surface forcing. The last two terms on the right-hand side, $(\partial \bar{T}_v/\partial t)_R$ and $(\partial \bar{T}_v/\partial t)_G$, are grid mean virtual temperature tendencies due to radiation and grid-scale advection. Traditionally, all microphysical processes for cumulus clouds are considered subgrid-scale and absorbed in $(dA/dt)_s$ or $M_b F$.

To determine $\overline{w'h'}_{ZM}$, we calculate mean state variables, mean radiative heating rates, and mean heating/moistening rates due to surface and PBL eddy fluxes for each subdomain in the CRM domain, as explained earlier. We also calculate grid-scale, i.e., subdomain-scale, advective tendencies of temperature and moisture from grid (subdomain) mean variables. Then we evaluate $(dA/dt)_g$ by calculating the change rate in A due to grid-scale advection, radiation, and surface and PBL eddy fluxes using equation (9). F is an output from the ZM mass flux model once the mean state variables are specified. Equation (8) then gives us M_b. With M_b, the ZM mass flux model produces $\overline{w'h'}_{ZM}$ using equation (6), as explained above (see also ZM and equations (3) and (8) therein).

The procedure we follow to calculate $\overline{w'h'}_{CRM}$ and $\overline{w'h'}_{ZM}$ is summarized in Figure 2. The calculation is repeated for all available temporal snapshots in each simulation. The maximum subdomain size we choose is 256 × 256 km^2 for DYNAMO and 128 × 128 km^2 for IDEAL, and the minimum is 8 × 8 km^2 for both simulations.

3. Results

We compare the resolution-dependent behavior of $\overline{w'h'}_{CRM}$ and $\overline{w'h'}_{ZM}$ for the following two aspects: (1) ensemble means, using angle brackets to indicate ensemble means over all subdomains, e.g., $\langle\overline{w'h'}_{CRM}\rangle$ and $\langle\overline{w'h'}_{ZM}\rangle$, and (2) probability density functions (PDFs). For the first aspect, we expect the ratio of $\langle\overline{w'h'}\rangle$ to the total transport $\langle\overline{w'h'} + \bar{w}\bar{h}\rangle$ to decrease as we reduce the subdomain size, i.e., increase the resolution, since more of the total transport becomes resolved. For our analysis based on CRM simulations, when the subdomain size is reduced to the CRM grid size, all transport is due to resolved motion and this ratio goes to zero (if we look at free troposphere levels and ignore contributions from CRM subgrid-scale turbulence parameterization). For the second aspect, we expect the shape of the PDF for $\overline{w'h'}$ to be flatter and have a longer tail for extreme values as we reduce subdomain size as found by, e.g., *Craig and Cohen* [2006].

3.1. Ensemble-Averaged Subgrid-Scale Vertical Transport

Figure 3 shows the vertical profiles of $\langle\overline{w'h'}_{CRM}\rangle$ and $\langle\overline{w'h'}_{ZM}\rangle$ for REAL and IDEAL. The ensemble mean is taken over the entire domain and for all available temporal snapshots. Please note that our definition of the

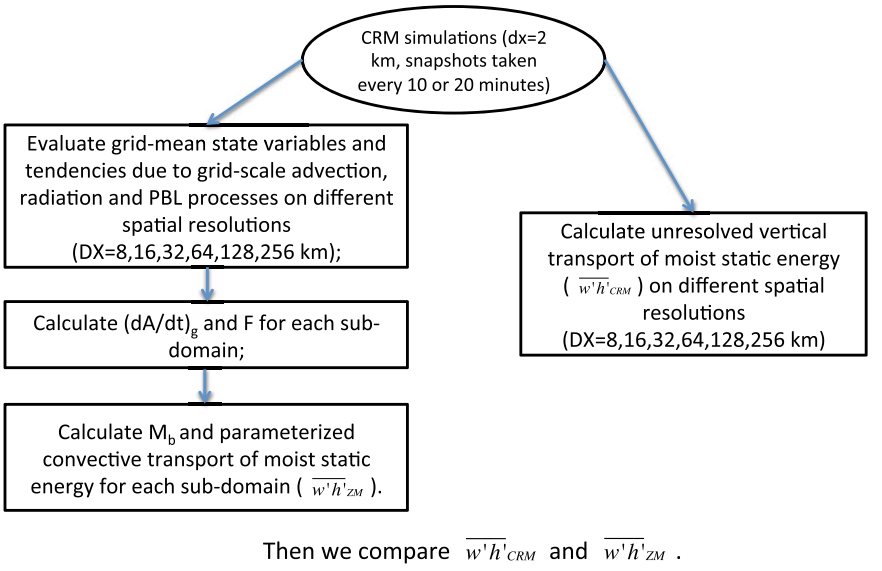

Figure 2. A schematic showing the procedure we follow to calculate $\overline{w'h'}_{ZM}$ and $\overline{w'h'}_{CRM}$.

ensemble mean is different from that in *Arakawa and Wu* [2013] who define their ensemble over subdomains with convective updrafts. With our definition the ensemble mean will always be over the same subdomains for $\overline{w'h'}_{CRM}$ and $\overline{w'h'}_{ZM}$ even if ZM does not trigger deep convection in all the right subdomains. The raw $\langle\overline{w'h'}_{ZM}\rangle$ is only half the magnitude of $\langle\overline{w'h'}_{CRM}\rangle$ for the largest subdomain size in both cases. This

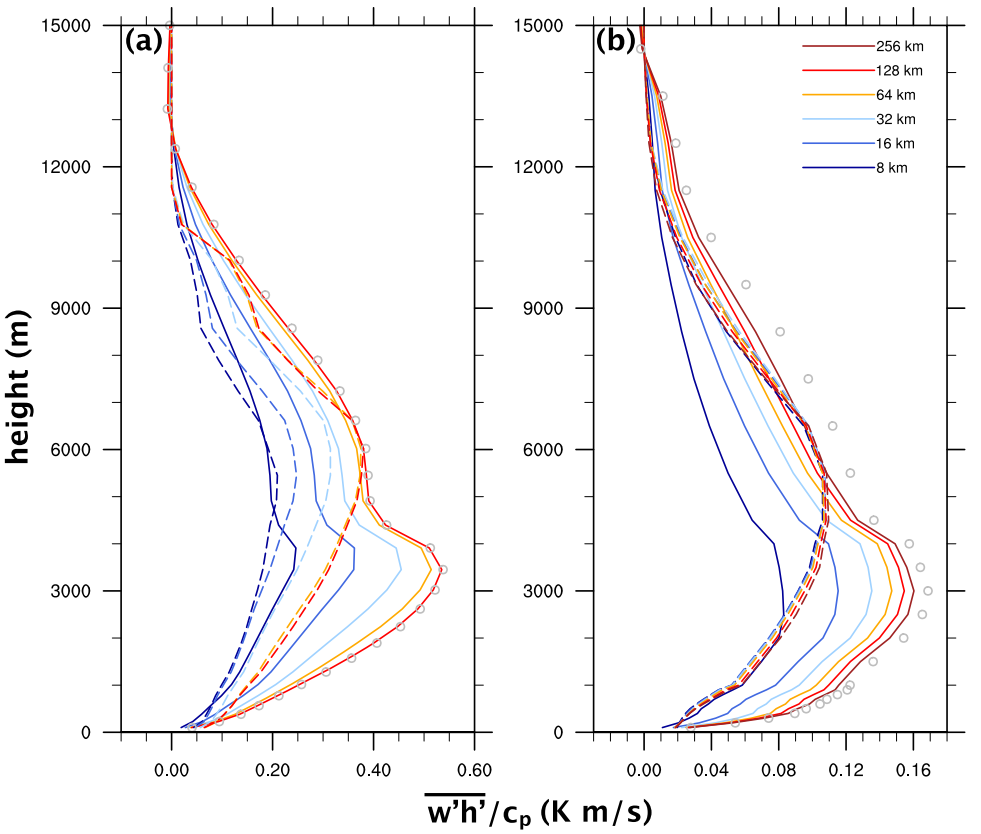

Figure 3. Vertical profiles of $\langle\overline{w'h'}_{CRM}\rangle$ (solid) and $\langle\overline{w'h'}_{ZM}\rangle$ (dashed) for the (a) IDEAL and (b) REAL case. Different colors indicate different subdomain sizes. $\langle\overline{wh}\rangle$ is indicated by gray circles for each case.

is likely caused by an overestimation of F in equation (8), i.e., the rate of CAPE consumption by unit mass flux, which could be due to discrepancies in the mass flux model. These discrepancies do not affect our analysis in the following which mainly focuses on $(dA/dt)_{g+}$ and $(dA/dt)_g$ (see also Figure 4 and our discussion thereof). Our conclusion concerning the convection closure in ZM is also quite independent of F and the details of the mass flux model. In Figure 3, in order to compare the resolution-dependent behavior of $\langle \overline{w'h'}_{CRM} \rangle$ and $\langle \overline{w'h'}_{ZM} \rangle$ more easily, we multiply the actual $\langle \overline{w'h'}_{ZM} \rangle$ by a constant (in the vertical and for all subdomain sizes) so that its value at the 6 km level is the same as that of $\langle \overline{w'h'}_{CRM} \rangle$ for the largest subdomain size (128 km for IDEAL and 256 km for REAL). The 6 km level is chosen because we take the convective transport through the middle troposphere as representative of the overall deep convection strength. Other notable differences between the ZM and CRM flux profiles are that (1) the depth of convection in ZM is underestimated by 1–2 km in both simulations; and (2) partly because the ZM scheme is designed to be a deep convection parameterization and no mass flux is allowed to detrain below the minimum moist static energy level in the middle troposphere, ZM misses the transport maximum due to convective elements that detrain before they reach the middle troposphere in both cases. Presumably, this missing part of the transport would be handled by a separate shallow convection scheme.

In Figure 3, we see that for both cases $\langle \overline{w'h'}_{CRM} \rangle$ behaves as we discussed above: for subdomain size of 128 or 256 km unresolved motion is responsible for most of the vertical transport within the domain, while for 8 km subdomain size it only accounts for about half of the total vertical transport through the middle troposphere (e.g., the 6 km level). Note the total vertical transport, $\langle \overline{w'h'}_{CRM} + \bar{w}\bar{h} \rangle$, does not change with changing subdomain size. On the other hand, the resolution dependence of $\langle \overline{w'h'}_{ZM} \rangle$ in Figure 3 shows an interesting difference between the two cases. For the REAL case (Figure 3b), there is almost no resolution dependence, i.e., ZM is double-counting vertical transport at high resolutions, but for the IDEAL case (Figure 3a) the decrease of $\langle \overline{w'h'}_{ZM} \rangle$ with decreasing subdomain size is quite realistic compared to the decrease of $\langle \overline{w'h'}_{CRM} \rangle$.

To further investigate the origin of the resolution dependence of $\langle \overline{w'h'}_{ZM} \rangle$, we compare the resolution-dependent behavior of $\langle \overline{w'h'}_{ZM} \rangle$ at the 6 km level with that of $\langle (dA/dt)_{g+} \rangle$ (see equation (8)) for both IDEAL and REAL in Figure 4. To produce Figure 4, the entire REAL simulation period is divided into 53 12 h segments, each the same length as IDEAL. This makes the comparison between IDEAL and REAL more direct and demonstrates the variability within the REAL simulation. These 12 h REAL segments are then sorted by their corresponding $\langle \overline{w'h'}_{CRM} \rangle$ (averaged over each 12 h segment), and grouped into quartiles. This way, the different quartiles represent the changing behavior across the range of convection strengths as measured by $\langle \overline{w'h'}_{CRM} \rangle$. Averages over individual quartiles are shown in light blue lines while the total ensemble (all quartiles) average is shown in dark blue. First of all, we see that, for both IDEAL and REAL, $\langle (dA/dt)_{g+} \rangle$ (Figure 4b) dictates the resolution-dependent behavior of $\langle \overline{w'h'}_{ZM} \rangle$ (Figure 4a). In other words, in the ZM scheme, the closure assumption (equation (8)) determines the resolution-dependence of $\langle \overline{w'h'} \rangle$. Second, different quartiles in REAL behave very differently: Quartile 4 with the largest $\langle \overline{w'h'}_{CRM} \rangle$ shows a similar though weaker decrease in $\langle \overline{w'h'}_{ZM} \rangle$ and $\langle (dA/dt)_{g+} \rangle$ with decreasing subdomain size compared to IDEAL while Quartile 1 with the smallest $\langle \overline{w'h'}_{CRM} \rangle$ shows a steep increase.

The resolution dependence of $\langle (dA/dt)_{g+} \rangle$ is quite different from that of $\langle (dA/dt)_g \rangle$ itself, which is shown in Figure 5a. IDEAL and the quartiles of REAL all show a consistent decrease of $\langle (dA/dt)_g \rangle$ with decreasing subdomain size. Furthermore, $\langle (dA/dt)_g \rangle$ displays a resolution-dependent behavior similar to $\langle \overline{w'h'}_{CRM} \rangle$ (Figure 5b), even though the spread is larger.

We can explain this similarity between $\langle (dA/dt)_g \rangle$ and $\langle \overline{w'h'}_{CRM} \rangle$ through equation (9). If we apply ensemble averaging to equation (9), we get

$$\left\langle \left(\frac{dA}{dt}\right)_g \right\rangle \approx \left\langle (\bar{T}_b - \bar{T}_t) \frac{c_p}{\bar{\theta}_{eb}} \frac{\partial \bar{\theta}_{eb}}{\partial t} \right\rangle - \left\langle R_d \int_{p_t}^{p_b} \left(\frac{\partial \bar{T}_v}{\partial t}\right)_R d\ln p \right\rangle - \left\langle R_d \int_{p_t}^{p_b} \left(\frac{\partial \bar{T}_v}{\partial t}\right)_G d\ln p \right\rangle. \tag{10}$$

Emanuel [1994, pp. 482–483] pointed out that in the tropical atmosphere the three terms on the right-hand side of equation (10) are usually of the same order of magnitude. The first two terms (due to surface warming/moistening and radiative cooling respectively) are usually positive and do not change with changing subdomain size. The third term, due to grid-scale advection, is dominated by vertical advection in the tropical atmosphere [see, e.g., *Emanuel*, 1994, pp. 483]. We can approximate this term as follows,

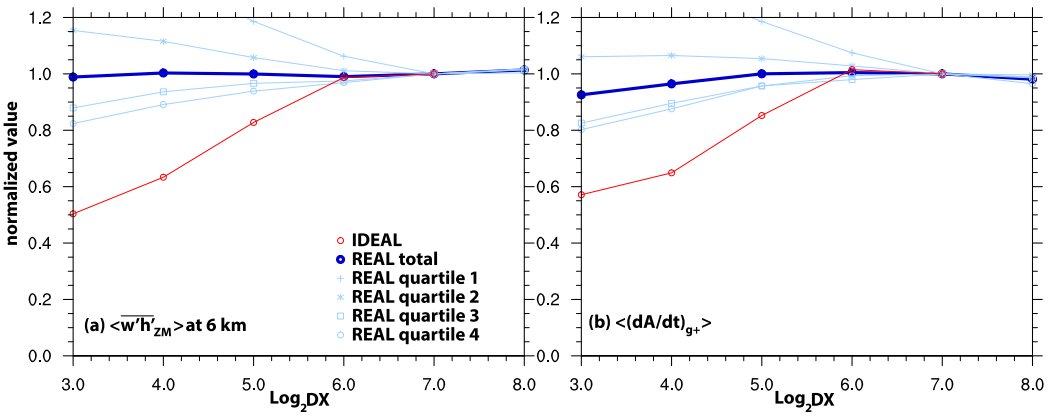

Figure 4. Scale dependence of (a) $\langle \overline{w'h'}_{ZM} \rangle$ at 6 km level and (b) $\langle (dA/dt)_{g+} \rangle$. The values for different subdomain sizes are normalized by the value for the subdomain size of 128 km (i.e., DX = 128 km). The quartiles of REAL are constructed according to the strength of convection measured by $\overline{w'h'}_{CRM}$ at the 6 km level. The forth quartile has the strongest convection strength. Please refer to the text for details of how the quartiles are constructed for the REAL case.

$$
\begin{aligned}
-\left\langle R_d \int_{p_t}^{p_b} \left(\frac{\partial \bar{T}_v}{\partial t}\right)_G d\ln p \right\rangle &= \left\langle \int_{z_b}^{z_t} \frac{g}{\bar{\theta}_v}\left[\frac{\partial(\bar{u}\bar{\theta}_v)}{\partial x} + \frac{\partial(\bar{v}\bar{\theta}_v)}{\partial y} + \frac{\partial(\bar{w}\bar{\theta}_v)}{\partial z}\right] dz \right\rangle \\
&= \left\langle \int_{z_b}^{z_t} \frac{g}{\bar{\theta}_v}\left[\frac{\partial(\overline{u\theta_v} - \overline{u'\theta'_v})}{\partial x} + \frac{\partial(\overline{v\theta_v} - \overline{v'\theta'_v})}{\partial y} + \frac{\partial(\overline{w\theta_v} - \overline{w'\theta'_v})}{\partial z}\right] dz \right\rangle \\
&\approx \left\langle \int_{z_b}^{z_t} \frac{g}{\theta_{v0}}\left(\frac{\partial \overline{u\theta_v}}{\partial x} + \frac{\partial \overline{v\theta_v}}{\partial y} + \frac{\partial \overline{w\theta_v}}{\partial z} - \frac{\partial \overline{w'\theta'_v}}{\partial z}\right) dz \right\rangle \\
&\approx \left\langle \int_{z_b}^{z_t} \frac{g}{\theta_{v0}}\left(\frac{\partial \overline{u\theta_v}}{\partial x} + \frac{\partial \overline{v\theta_v}}{\partial y} + \frac{\partial \overline{w\theta_v}}{\partial z}\right) dz \right\rangle + \frac{g}{\theta_{v0}} \langle \overline{w'\theta'_v}|_{z=z_b} \rangle,
\end{aligned}
\tag{11}
$$

where θ_v is the virtual potential temperature, θ_{v0} is the reference state virtual potential temperature, and z_t and z_b are the cloud top and base heights. The Boussinesq approximation is used. The divergence of horizontal eddy transports is assumed to be negligible and $\langle \overline{w'\theta'_v}|_{z=z_t} \rangle$ taken to be zero. Only the last term on the right-hand side of equation (11) varies with subdomain size and it decreases with subdomain size in a way similar to $\langle \overline{w'h'}_{CRM} \rangle$ (not shown). Ideally $\langle (dA/dt)_g \rangle$ could go to zero, like $\langle \overline{w'h'}_{CRM} \rangle$, when all the instability or the production of CAPE due to surface and radiative forcing (the first two terms on the right-hand side in equation (10)) are removed by resolved motion (the last term).

Why does $\langle (dA/dt)_{g+} \rangle$ behave differently from $\langle (dA/dt)_g \rangle$ as resolution increases? Comparing Figures 4b and 5a, we see that the difference between $\langle (dA/dt)_g \rangle$ and $\langle (dA/dt)_{g+} \rangle$ increases with decreasing subdomain size and decreasing strength of convection. This is because the possibility of having negative $(dA/dt)_g$ is bigger with smaller subdomain size and weaker overall convection. The ensemble average, $\langle (dA/dt)_g \rangle$, decreases as resolution increases but remains positive for convectively active regions. However, for each individual subdomain, as its size decreases, the chance of finding negative $(dA/dt)_g$ increases even for convectively active regions. This drives the increasing disparity between $\langle (dA/dt)_g \rangle$ and $\langle (dA/dt)_{g+} \rangle$, hence the increasing disparity between $\langle \overline{w'h'}_{CRM} \rangle$ and $\langle (dA/dt)_{g+} \rangle$, as resolution increases. Our interpretation of this disparity is that as resolution increases, QE holds less well over individual grid boxes: the chance of convectively active grid boxes (the activity measured by $\overline{w'h'}_{CRM}$) being associated with negative $(dA/dt)_g$ increases.

To remedy this disparity and to apply the QE-based closure at high resolutions in a way consistent with its presumption, we propose a simple algorithm to replicate the resolution awareness of $(dA/dt)_g$ when determining $\overline{w'h'}_{ZM}$: instead of using the local $(dA/dt)_g$ calculated in an individual subdomain, we use a spatial average of $(dA/dt)_g$, denoted as $\overline{(dA/dt)_g}$, over all subdomains in a large area centered on the subdomain for which the convective transport is being determined: 128 × 128 km^2 is used in the following calculations and we find small sensitivities when changing the averaging area to 64 × 64 km^2 or 256 ×256 km^2. The reasoning behind this design is that (1) we expect the explanation for the resolution

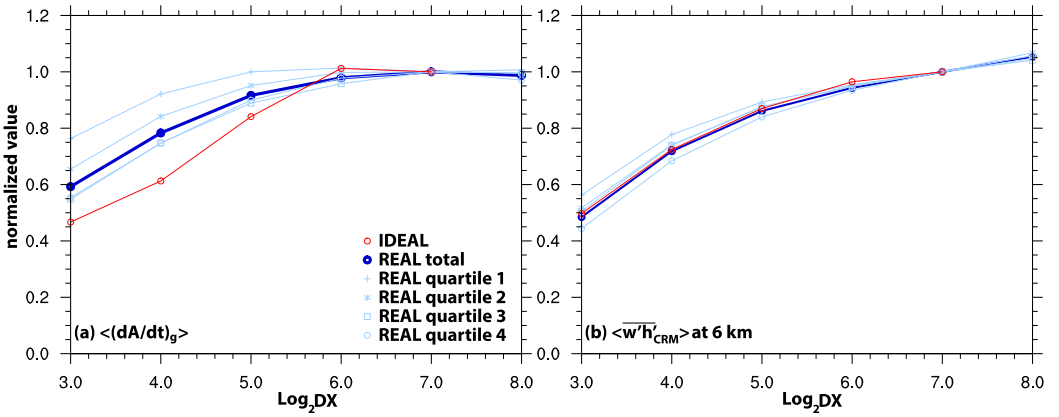

Figure 5. Scale dependence of (a) $\langle(dA/dt)_g\rangle$ and (b) $\langle\overline{w'h'}_{CRM}\rangle$ at 6 km level. The values for different subdomain sizes are normalized by the value for the subdomain size of 128 km (i.e., DX=128 km).

dependence of $\langle(dA/dt)_g\rangle$ through equations (10–11) to be generally applicable to $\overline{\overline{(dA/dt)}_g}$, (2) QE as expressed in equation (3) holds for the averaging area so that $\overline{(dA/dt)}_g$ will be positive for active convection regions. With this simple algorithm, we lose information about the grid-scale forcing at each grid box (which we cannot exploit within the QE framework) but $\overline{w'h'}_{ZM}$ calculated using $\overline{\overline{(dA/dt)}_g}$ represents the actual expected value from the QE closure. The closure equation (equation (8)) becomes,

$$M_b F = \left(\frac{dA}{dt}\right)_{gm+} \equiv \max\left[\overline{\overline{\left(\frac{dA}{dt}\right)}_g}, 0\right]. \tag{12}$$

$\overline{w'h'}_{ZM}$ calculated using this new closure will be denoted as $\overline{w'h'}_{ZM,m}$. Figure 6 shows the resolution dependence of $\langle\overline{w'h'}_{ZM,m}\rangle$ at the 6 km level. In both cases, the resolution dependence of $\langle(dA/dt)_g\rangle$ is reproduced in $\langle(dA/dt)_{gm+}\rangle$ and $\langle\overline{w'h'}_{ZM,m}\rangle$. For the REAL case, the resolution dependence of $\langle\overline{w'h'}_{ZM,m}\rangle$ is quite similar to that of $\langle\overline{w'h'}_{CRM}\rangle$: $\langle\overline{w'h'}_{ZM,m}\rangle$ decreases 40% as the subdomain size decreases from 128 to 8 km while $\langle\overline{w'h'}_{CRM}\rangle$ decreases 50%. For the IDEAL case, the good resolution-dependence with the original closure we see in Figure 4b is also reproduced by the new one. These results show that by using the simple averaging algorithm within the QE framework, we can, to a large extent, reproduce the changing partition between grid-scale and subgrid-scale vertical transport and therefore avoid the double-counting between these two.

The spread we see in $\langle(dA/dt)_g\rangle$ (Figure 5a) is still present in Figure 6 and the slope for the total ensemble average (the dark blue line) toward small subdomain size is less steep than that of $\langle\overline{w'h'}_{CRM}\rangle$ in Figure 5b (40 versus 50 % decrease from 128 to 8 km). We do not know the exact causes for these differences. One cause could be that the contribution from microphysical processes are all included in $(dA/dt)_s$, not explicitly in $(dA/dt)_g$. So even if subgrid-scale transport goes to zero, $(dA/dt)_s$ (and with it $(dA/dt)_g$) does not. This could lead to slower decrease of $\langle(dA/dt)_g\rangle$ than that of $\langle\overline{w'h'}_{CRM}\rangle$ when the subdomain size is reduced.

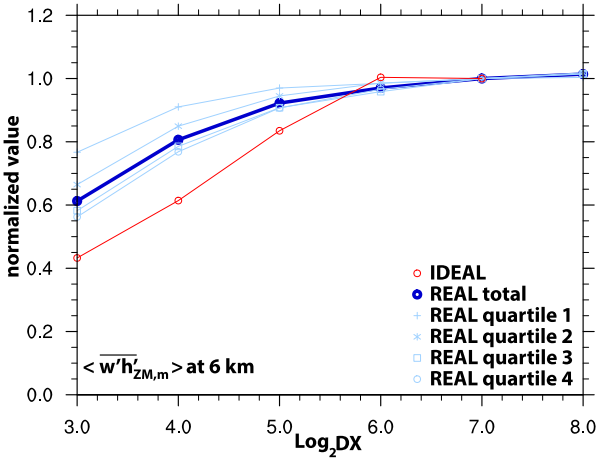

Figure 6. Scale dependence of $\langle\overline{w'h'}_{ZM,m}\rangle$ at 6 km level. The values for different subdomain sizes are normalized by the value for the subdomain size of 128 km (i.e., DX=128 km).

3.2. The PDFs

A good convection parameterization should reproduce not only the overall strength but also the variability of subgrid-scale vertical transport due to convection in terms of the PDF. A

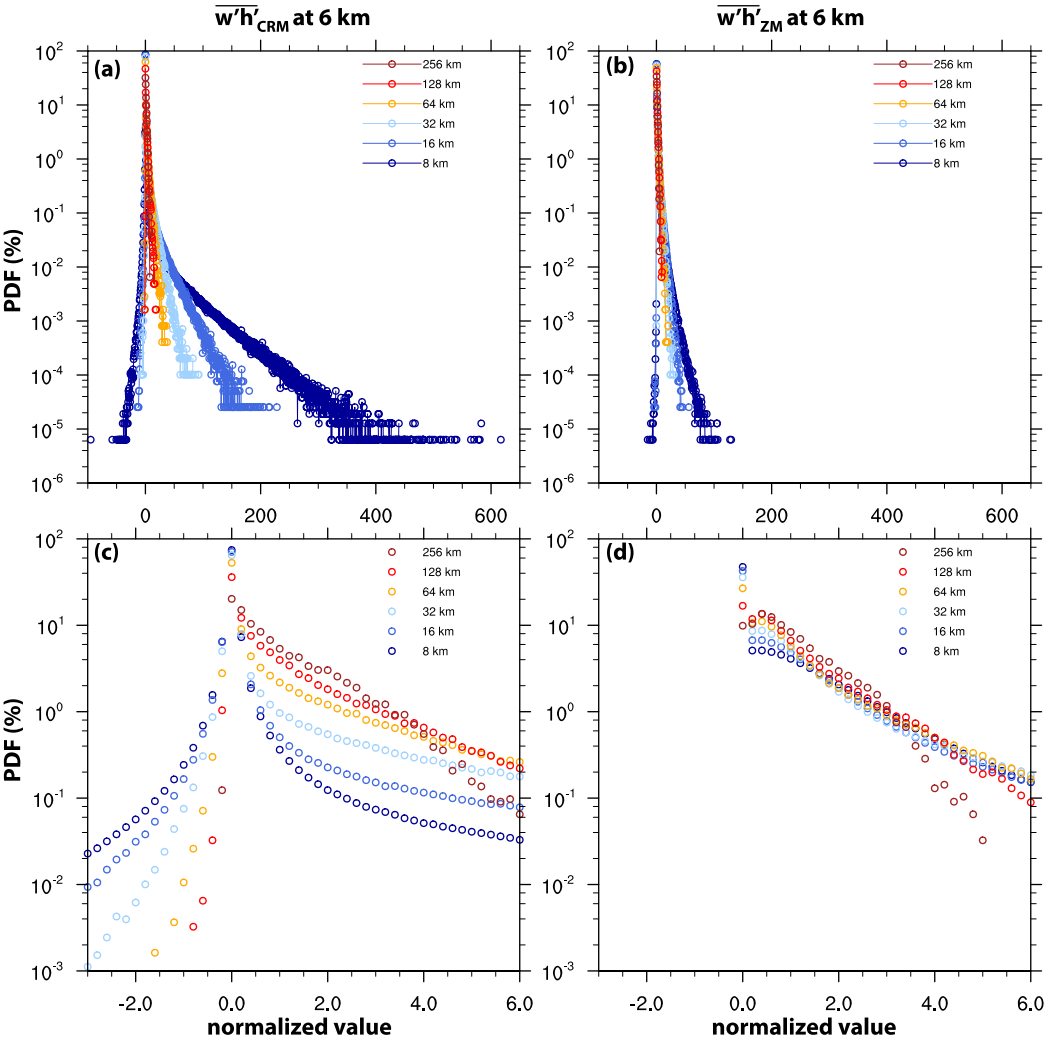

Figure 7. The PDFs of $\overline{w'h'}_{CRM}$ (a, c) and $\overline{w'h'}_{ZM}$ (b, d) at the 6 km level for the REAL case. (c) and (d) Blowups of (a) and (b) near $\overline{w'h'}=0$. The *x* axes are normalized by the ensemble average value.

common problem for convection parameterizations nowadays is the underestimation of such variability, hence the call for stochastic convection parameterizations [e.g., *Lin and Neelin*, 2003; *Buizza et al.*, 1999]. In this subsection, we compare the PDFs of $\overline{w'h'}_{ZM}$ and $\overline{w'h'}_{CRM}$ for different subdomain sizes.

Figure 7 shows the PDFs of $\overline{w'h'}_{ZM}$ and $\overline{w'h'}_{CRM}$ at the 6 km level for different subdomain sizes for the REAL case. The lower plots are blowups of the upper plots near the peak of the distribution. The general shape of the PDF of $\overline{w'h'}_{CRM}$ is quite comparable to those of convective heating in *Shutts and Palmer* [2007]. The change of the PDF of $\overline{w'h'}_{CRM}$ with changing subdomain size is also generally consistent with previous studies. For example, the increase in the probability density of zero convective eddy transport and the decrease of the probability density near the ensemble mean (i.e. near 1 on the normalized *x* axis in Figure 7c) with decreasing subdomain size can be seen in other CRM simulations [e.g., *Plant and Craig*, 2008, Figure 1 only the second feature] and theoretical calculations [e.g., *Keane and Plant*, 2012, Figure 16].

Table 1. Variance, Skewness and Kurtosis of Normalized $\overline{w'h'}_{CRM}$ and $\overline{w'h'}_{ZM}$ (bold values in parentheses) at 6 km Level for Different Subdomain Sizes for the REAL Case

Subdomain Size (km)	Variance	Skewness	Kurtosis
256	1.25 (**0.73**)	1.59 (**1.29**)	2.72 (**1.39**)
128	2.57 (**1.28**)	2.82 (**2.09**)	11.08 (**5.75**)
64	5.21 (**2.03**)	4.05 (**2.88**)	23.41 (**11.69**)
32	12.10 (**2.98**)	6.12 (**3.77**)	53.73 (**20.34**)
16	30.85 (**3.79**)	9.69 (**4.92**)	132.19 (**37.81**)
8	79.21 (**4.14**)	15.69 (**7.14**)	349.17 (**107.94**)

For $\overline{w'h'}_{ZM}$, we see from the upper plots that ZM underestimates the extension and magnitude of the PDF in the tail. This underestimation

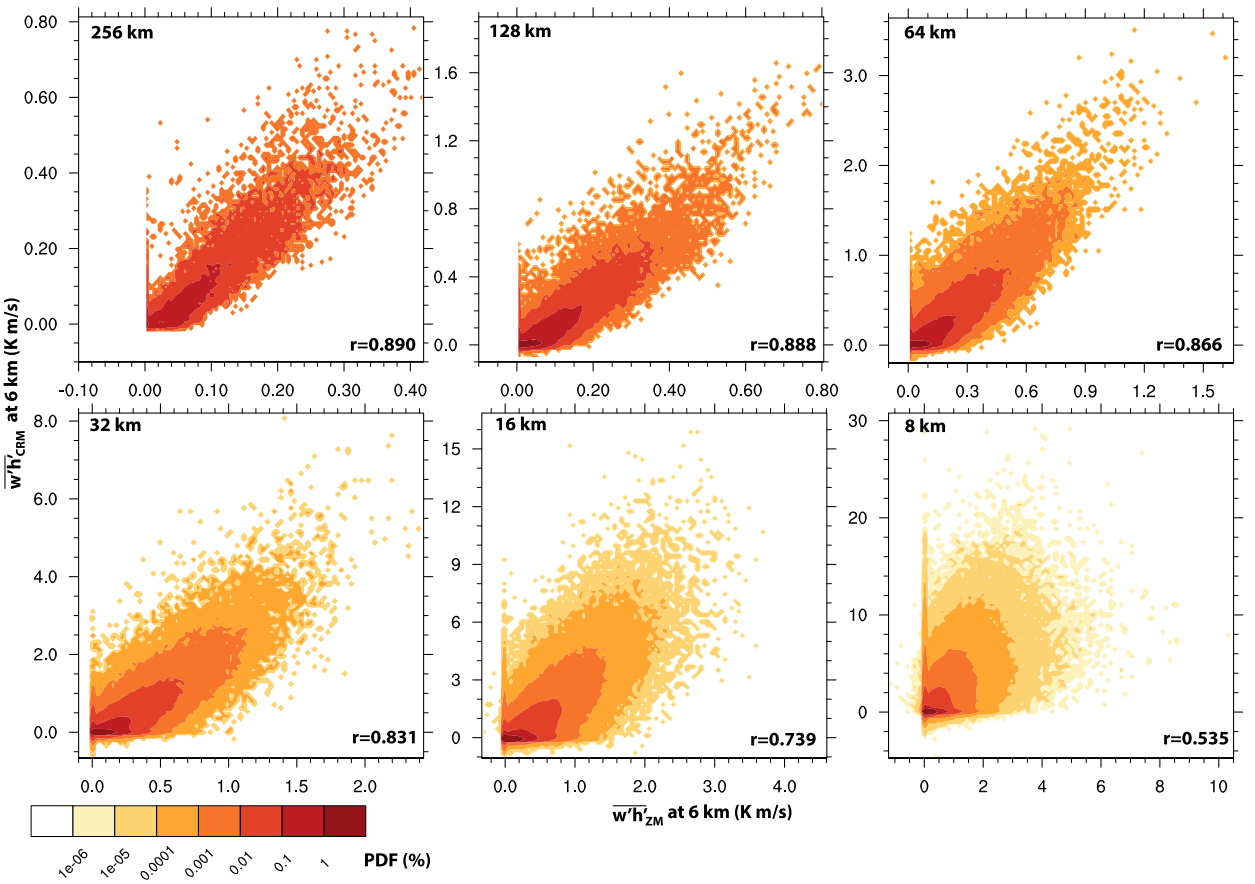

Figure 8. The two-dimensional PDF of $\overline{w'h'}_{CRM}$ and $\overline{w'h'}_{ZM}$ (both divided by c_p) at the 6 km level for the REAL case for different subdomain sizes. The correlation coefficients between $\overline{w'h'}_{CRM}$ and $\overline{w'h'}_{ZM}$ are displayed at the corner of each plot.

is quite drastic for small subdomain sizes (the blue lines). At 8 km grid spacing, the maximum of $\overline{w'h'}_{ZM}$ is more than 5 times smaller than that of $\overline{w'h'}_{CRM}$ even after normalization. In the lower plots, we see that, for $\overline{w'h'}_{CRM}$, as the subdomain size decreases from 256 to 8 km, the probability density near 1 (i.e., the mean value) decreases by almost two orders of magnitude. For $\overline{w'h'}_{ZM}$, however, the decrease is barely 50%. Table 1 lists the variance, skewness, and kurtosis of $\overline{w'h'}_{CRM}$ and $\overline{w'h'}_{ZM}$ at 6 km level normalized by their respective ensemble mean values for different subdomain sizes. The dramatic difference in terms of variance and kurtosis between $\overline{w'h'}_{CRM}$ and $\overline{w'h'}_{ZM}$ for 8 and 16 km subdomain sizes quantifies the differences we see in the PDF shape. We argue that the need for a stochastic formulation to better reproduce the realistic variability of subgrid-scale transport gets more important at higher resolution *for QE-based parameterizations* even though it is unclear from our analysis whether the difference in the PDFs is due to the deficiency of QE in capturing the deterministic portion (determined by grid-scale forcing) of the overall variability or the lack of nondeterministic variability (not determined by grid-scale forcing). Since the averaging algorithm suggested in the previous subsection leads to even narrower PDF shape (not shown), a stochastic formulation to enhance the variability would be even more desirable.

Even though the causal relationship behind equation (3) is difficult to elucidate, it has been shown by many studies [e.g., *Xu and Arakawa*, 1992] that parameterizations based on equation (3) perform well for large grid sizes in a diagnostic setup like ours. This can be seen in Figure 8. Figure 8 shows the joint PDFs of $\overline{w'h'}_{ZM}$ and $\overline{w'h'}_{CRM}$ at the 6 km level for different subdomain sizes for the REAL case. Note the magnitude difference between $\overline{w'h'}_{ZM}$ and $\overline{w'h'}_{CRM}$ discussed earlier. The correlation coefficient between $\overline{w'h'}_{ZM}$ and $\overline{w'h'}_{CRM}$ at the 6 km level is 0.89 for 128 and 256 km subdomain sizes. This correlation coefficient increases to 0.91 if we calculate the total CAPE change rate (dA/dt in equation (1)) for each subdomain and subtract it from $(dA/dt)_g$ following *Xu and Arakawa* [1992]. There are of course noticeable deficiencies even for large subdomain sizes. We see in all the plots (1) a spike at $\overline{w'h'}_{ZM}=0$, indicating that deep convection can

develop where the QE-based closure fails to "predict" any convection, and (2) a smoothed maximum along $\overline{w'h'}_{CRM}=0$ near the origin (i.e., for small $\overline{w'h'}_{ZM}$ values), suggesting that ZM tends to produce some weak convection where the CRM produces none. As we move toward higher resolution (smaller subdomain size), the correlation between $\overline{w'h'}_{ZM}$ and $\overline{w'h'}_{CRM}$ drops significantly; for a subdomain size of 8 km, the coefficient is only 0.54. In the plots for 8 and 16 km, the joint PDF looks like a spread fan, indicating bad point-by-point correlation. In other words, applying deterministic QE directly at high resolutions will not reproduce the variability of subgrid-scale transport even with "perfect" grid-scale input. We argue this is another justification for the use of a stochastic formulation to enhance the variability of subgrid-scale transport with QE-based parameterizations. Furthermore, it can be argued that with such bad correlation between simulated and parameterized subgrid-scale transport at high resolutions, potential degradation at individual points due to the averaging algorithm we proposed above is inconsequential. By adding stochastic formulations, we may be able to reproduce the overall variability of $\overline{w'h'}$.

4. Concluding Remarks

In this study, we have used a diagnostic approach to analyzing the resolution dependence of convective transport produced by the QE-based ZM convection parameterization. If we were to do the resolution-dependence analysis in a prognostic setup where we directly compare regular simulations running with the ZM parameterization and cloud microphysics/macrophysics parameterizations at different grid spacings, we would not be able to isolate the resolution dependence of convective transport from that of cloud microphysics/macrophysics. By feeding the convection scheme "perfect" grid-scale state variables diagnosed from CRM simulations, we also avoid amplification of errors due to known issues in the QE closure and the ZM scheme, e.g., deficiency in the triggering of convection (see Figure 8 and discussion thereof). Our diagnostic methodology enables us to temporarily ignore these issues and focus on a quantitative assessment of the resolution dependence of the subgrid-scale vertical transport produced by ZM. We find that,

1. Ensemble mean subgrid-scale vertical transport diagnosed from CRM simulations ($\overline{w'h'}_{CRM}$) decreases by more than half in magnitude as horizontal resolution increases from 256 to 8 km. This is consistent with previous studies [e.g., *Arakawa and Wu*, 2013; see also Figure 15 in *Arakawa and Jung*, 2011].
2. The resolution-dependent behavior of ensemble-averaged subgrid-scale vertical transport produced by ZM ($\overline{w'h'}_{ZM}$) is dictated by that of the positive-definite grid-scale CAPE tendency, $(dA/dt)_{g+}$, in the QE closure (equation (8)).
3. Ensemble-averaged $(dA/dt)_g$ decreases with increasing resolution, quite similar to the resolution-dependent behavior of $\overline{w'h'}_{CRM}$ while ensemble-averaged $(dA/dt)_{g+}$ decreases with increasing resolution only for strongly forced cases but increases steeply for relatively weakly forced cases. The similarity between $(dA/dt)_g$ and $\overline{w'h'}_{CRM}$ occurs because both of them are tied to the resolution dependence of grid-scale advective tendencies of temperature and moisture. The difference between $(dA/dt)_g$ and $(dA/dt)_{g+}$ is due to the increasing chance of $(dA/dt)_g$ becoming negative for individual subdomains as the subdomain size decreases (resolution increases) and the overall convection strength decreases, even though $(dA/dt)_g$ averaged over a large enough area (e.g., 128×128 km^2) remains positive.
4. A simple spatial averaging of $(dA/dt)_g$ over all subdomains over a large area (e.g., 128×128 km^2) around the subdomain of interest before taking its positive-definite value (equation (12)), can reproduce the resolution dependence of $(dA/dt)_g$ in $\overline{w'h'}_{ZM}$. This averaging links the subgrid-scale convective transport on the original grid (too fine for QE to hold) to the ensemble mean grid-scale forcing over a larger area over which QE can be consistently applied while retaining the resolution awareness of $(dA/dt)_g$ calculated on the original grid. It provides a simple but physically based way of avoiding double-counting of grid-scale and subgrid-scale vertical transport for QE-based convection parameterizations.
5. Underestimation of the variability of subgrid-scale vertical transport by ZM is more severe at higher resolutions and reproducing point-by-point the unresolved structure of convection at high resolutions (e.g., 8 km) is impossible with a deterministic QE closure.

Based on these findings, we emphasize the following two points for QE-based convection parameterizations. First, to avoid double-counting of resolved and parameterized vertical transport at "gray-zone" resolutions, we need modifications to the original QE closure. *Arakawa and Wu* [2013] propose that

double-counting can be avoided by incorporating a formulation for convective updraft fraction into a traditional convection parameterization. Our simple algorithm (point 4 above) also provides a way to avoid double-counting for diagnostic QE closures. Second, stochastic formulations like those of *Keane and Plant* [2012; see also *Plant and Craig*, 2008, *Keane et al*., 2014] and *Bengtsson et al*. [2013], which can produce realistic variability of subgrid-scale transport across different resolutions, may be necessary for QE-based parameterizations.

There are a few unresolved issues before our proposed algorithm can be implemented in a meaningful way in a QE-based convection parameterization for high-resolution models. First, we need to predict/diagnose the area fraction (i.e., we need to avoid the $\sigma \ll 1$ assumption) covered by convection so that microphysics formulations, like those by *Gerard et al*. [2007] and *Wu and Arawaka* [2014], can consistently handle convective and stratiform clouds coexisting in a single grid box given the fraction covered by each. Second, the algorithm we propose is based on diagnostic QE or so-called "strict" QE. Even though there are different views [e.g., *Kuang*, 2008], previous studies have argued for the importance of small time lags between convective adjustment and environmental processes [see, e.g., *Mapes*, 2000] and the need to avoid strict QE [e.g., *Khouider and Majda*, 2006] for realistic simulations of tropical convectively coupled waves and the MJO. Given our diagnostic methodology in the current study, accounting for such small time lags, e.g., by including the temporal tendencies of CAPE following *Xu and Arakawa* [1992], would not affect the overall performance of the ZM scheme in our diagnostic tests. We are currently exploring ways to incorporate our algorithm in a prognostic closure [e.g., *Pan and Randall*, 1998]. And last, we need to test the algorithm under a broader range of conditions, particularly in the midlatitudes to ensure its advantages are robust outside of the tropical regime tested in the current study.

Acknowledgments

Funding for H.X. and W.I.G. has been provided by a U. S. Department of Energy (DOE) Early Career grant awarded to W.I.G. S.M.H. acknowledges support from the Office of Biological and Environmental Research of the U. S. Department of Energy through its Atmospheric Systems Research Program and Regional and Global Climate Modeling Program. C.M.W. is supported by Taiwan's National Research Council through grants 101-2111-M-002–004 and 102-2111-M-002-003 to National Taiwan University. H.W. acknowledges support from the Linus Pauling Distinguished Postdoctoral Fellowship and the PNNL Laboratory Directed Research and Development program. Battelle Memorial Institute operates PNNL under contract DE-AC05-76RL01830. Computational resources were provided by the National Energy Research Scientific Computing (NERSC) Center, which is supported by the Office of Science of the U. S. Department of Energy under contract DE-AC02-05CH11231. Simulations are archived at NERSC (hopper.nersc.gov) and will be made available upon email request to the corresponding author (Heng.Xiao@pnnl.gov).

References

Arakawa, A. (2004), The cumulus parameterization problem: Past, present, and future, *J. Clim.*, *17*, 2493–2525.

Arakawa, A., and J.-H. Jung (2011), Multiscale modeling of the moist-convective atmosphere: A review, *Atmos. Res.*, *102*, 263–285, doi: 10.1016/j.atmosres.2011.08.009.

Arakawa, A., and W. Schubert (1974), Interaction of a cumulus cloud ensemble with the large-scale environment. Part I, *J. Atmos. Sci.*, *31*, 674–701.

Arakawa, A., and C.-M. Wu (2013), A unified representation of deep moist convection in numerical modeling of the atmosphere. Part I, *J. Atmos. Sci.*, *70*, 1977–1992, doi:10.1175/JAS-D-12-0330.1.

Bengtsson, L., M. Steinheimer, P. Bechtold, and J.-F. Geleyn (2013), A stochastic parametrization for deep convection using cellular automata, *Q. J. R. Meteorol. Soc.*, *139*, 1533–1543, doi:10.1002/qj.2108.

Bretherton, C. S., and S. Park (2009), A new moist turbulence parameterization in the community atmosphere model, *J. Climate*, *22*, 3422–3448.

Bryan G. H., J. C. Wyngaard, and J. M. Fritsch (2003), Resolution requirements for the simulation of deep moist convection, *Mon. Weather. Rev.*, *131*, 2394–2416.

Buizza, R., M. Miller, and T. N. Palmer (1999), Stochastic representation of model uncertainties in the ECMWF ensemble prediction scheme, *Q. J. R. Meteorol. Soc.*, *125*, 2887–2908, doi:10.1256/smsqj.56005.

Craig, G. C., and B. G. Cohen (2006), Fluctuations in an equilibrium convective ensemble. Part I, Theoretical formulation, *J. Atmos. Sci.*, *63*, 1996–2004.

Dudhia, J. (1989), Numerical study of convection observed during the winter monsoon experiment using a mesoscale two-dimensional model, *J. Atmos. Sci.*, *46*, 3077–3107.

Emanuel, K. A. (1994), *Atmospheric Convection*, Oxford Univ. Press, Oxford, U. K.

Gerard, L., J.-M. Piriou, R. Brožková, J.-F. Geleyn, and D. Banciu (2007), Cloud and precipitation parameterization in a meso-gamma-scale operational weather prediction model, *Mon. Weather. Rev.*, *137*, 3960–3977.

Hagos, S., Z. Feng, C. D. Burleyson, K.-S. S. Lim, C. N. Long, D. Wu, and G. Thompson (2014a), Evaluation of convection-permitting model simulations of cloud populations associated with the Madden-Julian Oscillation using data collected during the AMIE/DYNAMO field campaign, *J. Geophys. Res. Atmos.*, *119*, 12,052–12,068, doi:10.1002/2014JD022143.

Hagos, S., Z. Feng, K. Landu, and C. N. Long (2014b), Advection, moistening, and shallow-to-deep convection transitions during the initiation and propagation of Madden-Julian Oscillation, *J. Adv. Model. Earth Syst.*, *6*, 938–949, doi:10.1002/2014MS000335.

Huffman, G. J., R. F. Adler, D. T. Bolvin, G. Gu, E. J. Nelkin, K. P. Bowman, Y. Hong, E. F. Stocker, and D. B. Wolff (2007), The TRMM multisatellite precipitation analysis (TMPA): Quasi-global, multiyear, combined-sensor precipitation estimates at fine scales, *J. Hydrometeorol.*, *8*, 38–55.

Iacono, M. J., E. J. Mlawer, S. A. Clough, and J.-J. Morcrette (2000), Impact of an improved longwave radiation model, RRTM, on the energy budget and thermodynamic properties of the NCAR community climate model, *CCM3, J. Geophys. Res.*, *105*, 14,873–14,890, doi:10.1029/2000JD900091.

Jung, J.-H., and A. Arakawa (2004), The resolution dependence of model physics: Illustrations from nonhydrostatic model experiments, *J. Atmos. Sci.*, *61*, 88–102.

Jung, J.-H., and A. Arakawa (2008), A three-dimensional model based on the vorticity equation, *Mon. Weather Rev.*, *136*, 276–294.

Jung, J.-H., and A. Arakawa (2010) Development of a quasi-3d multiscale modeling framework: Motivation, basic algorithm and preliminary results, *J. Adv. Model. Earth Syst.*, *2*, 11, 1–31, doi:10.3894/JAMES.2010.2.11.

Keane R. J., and R. S. Plant (2012), Large-scale length and time-scales for use with stochastic convective parametrization, *Q. J. R. Meteorol. Soc.*, *138*, 1150–1164, doi:10.1002/qj.992.

Keane R. J., G. C. Craig, C. Keil, and G. Zängl (2014), The Plant-Craig stochastic convection scheme in ICON and its scale adaptivity, *J. Atmos. Sci.*, *71*, 3404–3415, doi:10.1175/JAS-D-13-0331.1.

Khouider, B., and A. J. Majda (2006), A simple multicloud parameterization for convectively coupled tropical waves. Part I: Linear analysis, *J. Atmos. Sci.*, *63*, 1308–1323.

Krueger, S. K., Q. Fu, K. N. Liou, and H.-N. Chin (1995), Improvements of an ice-phase microphysics parameterization for use in numerical simulations of tropical convection, *J. Appl. Meteorol.*, *34*, 281–287.

Kuang, Z. (2008), A moisture-stratiform instability for convectively coupled waves, *J. Atmos. Sci.*, *65*, 834–854.

Lin, J. W.-B., and J. D. Neelin (2003), Towards stochastic deep convective parameterization in general circulation models, *Geophys. Res. Lett.*, *30*(4), 1162, doi:10.1029/2002GL016203.

Lord, S. J. (1982), Interaction of a cumulus cloud ensemble with the large-scale environment. Part III: Semi-prognostic test of the Arakawa-Schubert cumulus parameterization, *J. Atmos. Sci.*, *39*, 88–103.

Lord, S. J. and A. Arakawa (1980), Interaction of a cumulus cloud ensemble with the large-scale environment. Part II, *J. Atmos. Sci.*, *37*, 2677–2692.

Mapes, B. E. (1997), Equilibrium vs. activation controls on large- scale variations of tropical deep convection, in *The Physics and Parameterization of Moist Atmospheric Convection*, edited by R. K. Smith, pp. 321–358, Kluwer Acad., Dordrecht, Netherlands.

Mapes, B. E. (2000), Convective inhibition, subgrid-scale triggering energy, and stratiform instability in a toy tropical wave model, *J. Atmos. Sci.*, *57*, 1515–1535.

Morrison, H., J. A. Curry, and V. I. Khvorostyanov (2005), A new double moment microphysics parameterization for application in cloud and climate models. Part I: Description, *J. Atmos. Sci.*, *62*, 1665–1677, doi:10.1175/JAS3446.1.

Neelin, J. D., O. Peters, J. W.-B. Lin, K. Hales, and C. E. Holloway (2008), Rethinking convective quasi-equilibrium: Observational constraints for stochastic convective schemes in climate models, *Philos. Trans. R. Soc. A*, *366*, 2581–2604.

Pan D.-M., and D. A. Randall (1998) A cumulus parameterization with a prognostic closure, *Q. J. R. Meteorol. Soc.*, *124*, 949–981.

Plant, R. S., and G. C. Craig (2008), A stochastic parameterization for deep convection based on equilibrium statistics, *J. Atmos. Sci.*, *65*, 87–105.

Shutts, G. J., and T. N. Palmer (2007), Convective forcing fluctuations in a cloud-resolving model: Relevance to the stochastic parameterization problem, *J. Clim.*, *20*, 187–202, doi:10.1175/JCLI3954.1.

Skamarock, W. C., J. B. Klemp, J. Dudhia, D. O. Gill, D. M. Barker, M. G. Duda, X.-Y. Huang, W. Wang, and J. G. Powers (2008), A description of the Advanced Research WRF version 3 *NCAR Tech. Note 475*., Mesoscale and Microscale Meteorology Division, National Center for Atmospheric Research, Boulder, Colo.

Williams, P. D. (2005), Modelling climate change: The role of unresolved processes, *Phil. Trans. R. Soc. A*, *363*, 2931–2946, doi:10.1098/rsta.2005.1676.

Wu, C.-M., and A. Arakawa (2014), A unified representation of deep moist convection in numerical modeling of the atmosphere. Part II, *J. Atmos. Sci.*, *71*, 2089–2103, doi:10.1175/JAS-D-13-0382.1.

Xu, K.-M., and A. Arakawa (1992), Semiprognostic test of the Arakawa-Schubert cumulus parameterization using simulated data, *J. Atmos. Sci.*, *49*(24), 2421–2436.

Yano, J.-I., and R. S. Plant (2012), Convective quasi-equilibrium, *Rev. Geophys.*, *50*, RG4004, doi:10.1029/2011RG000378.

Yano, J.-I., W. W. Grabowski, G. L. Roff, and B. E. Mapes (2000), Asymptotic approaches to convective quasi-equilibrium, *Q. J. R. Meteorol. Soc.*, *126*, 1861–1887.

Yoneyama, K., C. Zhang, and C. N. Long (2013), Tracking pulses of the Madden-Julian oscillation, *Bull. Am. Meteorol. Soc.*, *94*, 1871–1891, doi:10.1175/BAMS-D-12-00157.1.

Zhang, G. (2003), Convective quasi-equilibrium in the tropical western Pacific: Comparison with midlatitude continental environment, *J. Geophys. Res.*, *108*(D19), 4592, doi:10.1029/2003JD003520.

Zhang, G., and N. A. McFarlane (1995), Sensitivity of climate simulations to the parameterization of cumulus convection in the Canadian Climate Centre General Circulation Model, *Atmos. Ocean*, *33*, 407–446.